Int J Fract (2007) 143:207–217
DOI 10.1007/s10704-006-9016-7

ORIGINAL PAPER

Analysis of moiré data for near-interface cracks

Keith Rozenburg · J. R. Berger · P. A. Martin · Ivar Reimanis

Received: 20 July 2005 / Accepted: 11 September 2006 / Published online: 17 April 2007

Abstract The analysis of moiré data obtained in bimaterials with near-interface cracks is examined. To extract stress intensity factors, a collocation-type method is developed where Westergaard crack-tip expansions are used for displacements in the cracked portion of the bimaterial, expansions from the method of fundamental solutions are used for displacements in the uncracked portion of the bimaterial, and continuity conditions at the interface are used to couple the two expansions. Proof-of-principle numerical experiments performed on synthetic data from a boundary element analysis of a cracked bimaterial successfully demonstrated the analysis method. Mixed-mode stress intensity factors were then determined from actual moiré data obtained in a copper–tungsten specimen.

K. Rozenburg · I. Reimanis
Department of Metallurgical and Materials Engineering,
Colorado School of Mines, Golden,
CO 80401, USA

J. R. Berger (✉)
Division of Engineering,
Colorado School of Mines, Golden,
CO 80401, USA
e-mail:jberger@mines.edu

Present address:
J. R. Berger
School of Engineering, University of Alaska Anchorage,
Anchorage, AK 99502, USA

P. A. Martin
Department of Mathematical and Computer Sciences,
Colorado School of Mines, Golden,
CO 80401, USA

Keywords Moiré · Near-interface cracks · Collocation

1 Introduction

A variety of optical methods of experimental mechanics have been used successfully to measure the stress intensity factor at a crack tip. Methods such as photoelasticity (Dally 1979; Etheridge and Dally 1977; Sanford and Dally 1979; Schroedl and Smith 1975) and caustics (Rosakis and Zehnder 1985; Theocaris and Gdoutos 1972; Kalthoff 1987) have been extensively applied to both stationary and propagating cracks to extract stress intensity factors in both the opening mode, K_{I}, and the forward shear mode, K_{II}. The advantage of these methods is the determination of either the stress intensity factor or the fracture toughness directly from the experiment. This is especially useful when the experiments being analyzed are non-standard and no readily available formulas are available for determining the stress intensity factor from measured load and displacement data.

Moiré methods are another optical technique which have been widely used for the analysis of crack-tip stress fields. Moiré methods rely on the geometric interference between a deforming grating and a fixed grating to generate quantitative, full-field displacement data.

The fixed grating may be a physical grating, or may be generated by the interference between two mutually coherent beams of laser light (Epstein and Dadkhan 1993). The latter technique is commonly referred to as moiré interferometry. The moiré method has also been employed in a scanning electron microscope (Dally and Read 1993) where electron-beam lithography is used to generate the specimen grating and the scanning motion of the electron beam in the microscope naturally forms a reference grating. Electron-beam moiré has been used to study fracture of fiber reinforced plastics (Read and Dally 1994) and the mechanical behavior of conductive adhesives (Drexler and Berger 1999).

One difficulty in terms of the analysis of displacement data obtained by moiré methods is the wealth of data available from a particular experiment. Barker et al. (1985), developed a linear least-squares method to extract the opening mode stress intensity factor, K_{I}, from the measured displacement fields. The displacement field around the crack tip was written using generalized Westergaard expansions (Sanford 1979), which are equivalent to the usual Williams expansions (Williams 1957). The unknown coefficients in the displacement field expansions are determined through least squares fitting to the displacement data. The effects of rigid body rotations, uncertainty in crack-tip location, and the degree of redundancy in the data were all investigated in Barker et al. (1985).

In this paper, we extend the method of Barker et al. (1985) to problems involving a cracked bimaterial. In particular, we are interested in the analysis of moiré data obtained around a crack tip which is in close proximity to the interface between the two parts of the bimaterial. Some of the moiré data available for analysis is in the uncracked portion of the bimaterial; however, the Westergaard expansions are only valid in the material containing the crack. These solutions will not satisfy the continuity requirements on displacement and traction across the interface, so they are not valid in the uncracked portion of the bimaterial. We use expressions for the displacements in the uncracked portion of the bimaterial determined from the expansions used in the *Method of Fundamental Solutions* (MFS) (Fairweather and Karageorghis 1998). The MFS is a meshfree numerical method which has been applied to a variety of problems including harmonic and biharmonic boundary value problems (Poullikkas et al. 1998), potential, Helmholtz and diffusion problems (Golberg and Chen 1999), and elasticity problems (Berger and Karageorghis 2001). Here, we use the MFS expansions for displacement in the uncracked material, the Westergaard expansions for displacement in the cracked material, and enforce continuity conditions across the interface between the two materials. The continuity conditions then serve to couple these two expansions. We then use a linear least-squares method to determine the coefficients in the two expansions from the moiré data. Knowledge of the coefficients allows us to calculate the stress intensity factor(s), the T-stress, and other stress-field related parameters.

We will demonstrate the developed methodology on two example problems. In the first example, we generate synthetic moiré data using a boundary element analysis of a cracked bimaterial. The results show good convergence for K_{I} values as the number of terms in the expansions are increased. For the second example, we apply the methodology to experimental moiré data obtained from a copper–tungsten bimaterial specimen loaded in bending. Again the results for K_{I}, and also K_{II} in this example, show good convergence with very low least-squares residuals.

2 The MFS

We first consider the displacement field in the uncracked portion of the bimaterial shown in Fig. 1 (material A). We assume the material is isotropic with Poisson's ratio ν, so in the absence of body forces the displacements u_1 and u_2 are governed by the Navier equations,

$$(\lambda + \mu)u(P)_{i,ij} + \mu u(P)_{i,jj} = 0 \quad i, j = 1, 2, \tag{1}$$

where λ and μ are the Lamé constants, P is the calculation point for the displacements, $P = (x_{1_P}, x_{2_P})$, and the usual summation convention is implied over repeated indices. The strains $\varepsilon_{ij}, i, j = 1, 2$, are related to the displacement gradients by

$$\varepsilon_{ij} = \frac{1}{2}\left(\frac{\partial u_i}{\partial x_j} + \frac{\partial u_j}{\partial x_i}\right), \tag{2}$$

and the stresses $\sigma_{ij}, i, j = 1, 2$, are related to the strains through Hooke's law by

$$\sigma_{ij} = \lambda\delta_{ij}\varepsilon_{kk} + 2\mu\varepsilon_{ij}, \tag{3}$$

where δ_{ij} is the Kronecker delta. The fundamental solutions of the system of Eq. 1, which physically represent the displacement field due to a point load in the solid, are given by the two-point functions

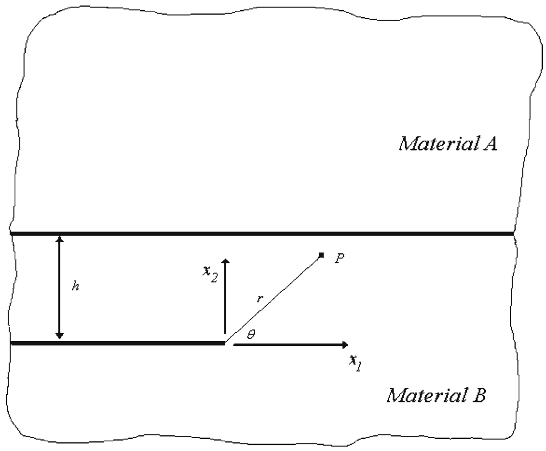

Fig. 1 Cracked bimaterial specimen

$$G_{11}(P, Q) = (3 - 4\nu) \log r_{PQ} - \frac{(x_{1_P} - x_{1_Q})^2}{r_{PQ}^2}, \quad (4)$$

$$G_{12}(P, Q) = G_{21}(P, Q) = \frac{(x_{1_P} - x_{1_Q})(x_{2_P} - x_{2_Q})}{r_{PQ}^2}, \quad (5)$$

$$G_{22}(P, Q) = (3 - 4\nu) \log r_{PQ} - \frac{(x_{2_P} - x_{2_Q})^2}{r_{PQ}^2}, \quad (6)$$

where Q is the location of the point load, $Q = (x_{1_Q}, x_{2_Q})$, and

$$r_{PQ} = \sqrt{(x_{1_P} - x_{1_Q})^2 + (x_{2_P} - x_{2_Q})^2}.$$

Note in Eqs. 4–6 that some constant factors premultiplying the G_{ij} terms have been dropped; however, these constants are absorbed in the coefficients of the expansions taken below.

In the MFS, the displacements are approximated by a linear combination of fundamental solutions as

$$u_1(P) = \sum_{n=1}^{N} a_n G_{11}(P, Q_n) + \sum_{n=1}^{N} b_n G_{12}(P, Q_n), \quad (7)$$

$$u_2(P) = \sum_{n=1}^{N} a_n G_{21}(P, Q_n) + \sum_{n=1}^{N} b_n G_{22}(P, Q_n), \quad (8)$$

where $\mathbf{a} = (a_1, a_2, \ldots, a_N)$, $\mathbf{b} = (b_1, b_2, \ldots, b_N)$ and $\mathbf{Q}$ is a $2N$-vector containing the coordinates of the point sources Q_j, which lie *outside* the physical domain of the problem. Since the calculation point, P, and the source points, Q_j, are never coincident, the log terms in the fundamental solutions, Eqs. 4–6, are never singular. In the standard MFS, a set of points $\{P_i\}_{i=1}^{M}$ is selected on the boundary of the physical domain and the coefficients $\mathbf{a}$,$\mathbf{b}$ and the locations of the sources $\mathbf{Q}$ are determined by minimizing the functional

$$F(\mathbf{a}, \mathbf{b}, \mathbf{Q}) = \sum_{i=1}^{M} |B_1[u_1, u_2, t_1, t_2](P_i) - f_1(P_i)|^2 + |B_2[u_1, u_2, t_1, t_2](P_i) - f_2(P_i)|^2, \quad (9)$$

where the operators B_1 and B_2 specify displacement, traction or mixed boundary conditions and $f_1(P)$, $f_2(P)$ are the prescribed boundary values. If needed, the expansions for the tractions t_1 and t_2 are obtained from the expansions for the displacement field. The minimization of the functional in Eq. 9 to determine $\mathbf{a}$, $\mathbf{b}$, and $\mathbf{Q}$ is performed by minimizing the sum of squares of m non-linear functions in n variables using a modified version of the Levenberg–Marquard algorithm.

Alternatively, the locations of the sources $\mathbf{Q}$ may be *prescribed*. In this case, a linear least-squares problem is obtained in the coefficients $\mathbf{a}$,$\mathbf{b}$. This is the technique we will use for the displacements in the uncracked portion of the bimaterial. Movable sources could be included in future investigations, but we shall see that the simpler algorithm based on prescribed source locations is effective.

3 Generalized Westergaard expansions near a crack tip

We next consider the displacements in the cracked portion of the bimaterial, material B in Fig. 1. For a mode I crack, Sanford (Sanford 1979) generalized the Westergaard stress function approach to crack problems (Westergaard 1939) in terms of two complex-valued functions $Z_{\mathrm{I}}(z)$ and $Y_{\mathrm{I}}(z)$ as

$$\sigma_{11} = \operatorname{Re} Z_{\mathrm{I}}(z) - x_2 \left[\operatorname{Im} Z'_{\mathrm{I}}(z) + \operatorname{Im} Y'_{\mathrm{I}}(z) \right] + 2 \operatorname{Re} Y_{\mathrm{I}}(z), \quad (10)$$

$$\sigma_{22} = \operatorname{Re} Z_{\mathrm{I}}(z) + x_2 \left[\operatorname{Im} Z'_{\mathrm{I}}(z) + \operatorname{Im} Y'_{\mathrm{I}}(z) \right], \quad (11)$$

$$\sigma_{12} = -\operatorname{Im} Y_{\mathrm{I}}(z) - x_2 \left[\operatorname{Re} Z'_{\mathrm{I}}(z) + \operatorname{Re} Y'_{\mathrm{I}}(z) \right]. \quad (12)$$

Substituting these stresses into Hooke's law, Eq. 3, and integrating the strain–displacement equations, Eq. 2, yields the displacements

$$E u_{1,\mathrm{I}} = (1 - \nu) \operatorname{Re} \widetilde{Z}_{\mathrm{I}}(z) - (1 + \nu)\, x_2 [\operatorname{Im} Z_{\mathrm{I}}(z) + \operatorname{Im} Y_{\mathrm{I}}(z)] + 2 \operatorname{Re} \widetilde{Y}_{\mathrm{I}}(z), \quad (13)$$

$$Eu_{2,\mathrm{I}} = 2\,\mathrm{Im}\,\widetilde{Z}_{\mathrm{I}}(z) - (1+\nu)\,x_2[\,\mathrm{Re}\,Z_{\mathrm{I}}(z) + \mathrm{Re}\,Y_{\mathrm{I}}(z)] + (1-\nu)\,\mathrm{Im}\,\widetilde{Y}_{\mathrm{I}}(z), \tag{14}$$

where

$$\widetilde{Z}_{\mathrm{I}}(z) = \int Z_{\mathrm{I}}(z)\,\mathrm{d}z, \quad \widetilde{Y}_{\mathrm{I}}(z) = \int Y_{\mathrm{I}}(z)\,\mathrm{d}z$$

the subscript I indicates mode I, and E is Young's modulus. For mode II, the generalized Westergaard stresses are Sanford (2003)

$$\sigma_{11} = \mathrm{Im}\,Y_{\mathrm{II}}(z) - x_2\left[\,\mathrm{Re}\,Y'_{\mathrm{II}}(z) + \mathrm{Re}\,Z'_{\mathrm{II}}(z)\right] + 2\,\mathrm{Im}\,Z_{\mathrm{II}}(z), \tag{15}$$

$$\sigma_{22} = \mathrm{Im}\,Y_{\mathrm{II}}(z) + x_2\left[\,\mathrm{Re}\,Y'_{\mathrm{II}}(z) + \mathrm{Re}\,Z'_{\mathrm{II}}(z)\right], \tag{16}$$

$$\sigma_{12} = \mathrm{Re}\,Z_{\mathrm{II}}(z) - x_2\left[\,\mathrm{Im}\,Y'_{\mathrm{II}}(z) + \mathrm{Im}\,Z'_{\mathrm{II}}(z)\right]. \tag{17}$$

Again substituting these stresses into Hooke's law and integrating the strain–displacement equations yields the mode II displacements

$$Eu_{1,\mathrm{II}} = (1-\nu)\,\mathrm{Im}\,\widetilde{Y}_{\mathrm{II}}(z) + (1+\nu)\,x_2[\,\mathrm{Re}\,Y_{\mathrm{II}}(z) + \mathrm{Re}\,Z_{\mathrm{II}}(z)] + 2\,\mathrm{Im}\,\widetilde{Z}_{\mathrm{II}}(z), \tag{18}$$

$$Eu_{2,\mathrm{II}} = -2\,\mathrm{Re}\,\widetilde{Y}_{\mathrm{II}}(z) - (1+\nu)\,x_2[\,\mathrm{Im}\,Y_{\mathrm{II}}(z) + \mathrm{Im}\,Z_{\mathrm{II}}(z)] - (1-\nu)\,\mathrm{Re}\,\widetilde{Z}_{\mathrm{II}}(z). \tag{19}$$

For single-ended crack problems, the appropriate form of the mode I and mode II stress functions are

$$Z_{\mathrm{I}}(z) = \sum_{j=0}^{J} A_j z^{j-1/2}, \quad Z_{\mathrm{II}}(z) = \sum_{j=0}^{J} C_j z^{j-1/2}, \tag{20}$$

$$Y_{\mathrm{I}}(z) = \sum_{m=0}^{M} B_m z^m, \quad Y_{\mathrm{II}}(z) = \sum_{m=0}^{M} D_m z^m. \tag{21}$$

Substituting Eqs. 20 and 21 in Eqs. 13–14 and Eqs. 18-19, and then superposing the results yields the series expansions for the mixed-mode displacements,

$$Eu_1(r,\theta) = \sum_{j=0}^{J} r^{j+1/2}\left[A_j\, f_j(\theta) + C_j\, p_j(\theta)\right] + \sum_{m=0}^{M} r^{m+1}\left[B_m\, g_m(\theta) + D_m\, q_m(\theta)\right], \tag{22}$$

$$Eu_2(r,\theta) = \sum_{j=0}^{J} r^{j+1/2}\left[A_j\, h_j(\theta) + C_j\, s_j(\theta)\right] + \sum_{m=0}^{M} r^{m+1}\left[B_m\, k_m(\theta) + D_m\, t_m(\theta)\right], \tag{23}$$

where (r,θ) are local polar coordinates situated at the crack tip and

$$f_j(\theta) = \frac{1-\nu}{j+1/2}\cos\left(j+\frac{1}{2}\right)\theta - (1+\nu)\sin\theta\,\sin\left(j-\frac{1}{2}\right)\theta, \tag{24}$$

$$g_m(\theta) = \frac{2}{m+1}\cos(m+1)\theta - (1+\nu)\sin\theta\,\sin m\theta, \tag{25}$$

$$p_j(\theta) = (1+\nu)\sin\theta\,\cos\left(j-\frac{1}{2}\right)\theta + \frac{2}{j+1/2}\sin\left(j-\frac{1}{2}\right)\theta, \tag{26}$$

$$q_m(\theta) = \frac{1-\nu}{m+1}\sin(m+1)\theta + (1+\nu)\sin\theta\,\cos m\theta, \tag{27}$$

$$h_j(\theta) = \frac{2}{j+1/2}\sin\left(j+\frac{1}{2}\right)\theta - (1+\nu)\sin\theta\,\cos\left(j-\frac{1}{2}\right)\theta, \tag{28}$$

$$k_m(\theta) = \frac{1-\nu}{m+1}\sin(m+1)\theta - (1+\nu)\sin\theta\,\cos m\theta, \tag{29}$$

$$s_j(\theta) = -\frac{1-\nu}{j+1/2}\cos\left(j+\frac{1}{2}\right)\theta - (1+\nu)\sin\theta\,\sin\left(j-\frac{1}{2}\right)\theta, \tag{30}$$

$$t_m(\theta) = -\frac{2}{m+1}\cos(m+1)\theta - (1+\nu)\sin\theta\,\sin m\theta. \tag{31}$$

The displacement fields of Eqs. 22 and 23 are valid in the portion of the bimaterial containing the crack. In the next section, we link these displacement components with the MFS displacement fields for the uncracked portion of the bimaterial.

4 Coupling of the Westergaard and MFS expansions

We now consider the data collected in a typical moiré experiment in a cracked bimaterial. With reference to Fig. 1, we locate the origin of our coordinate system at the tip of the crack in material B and the interface is located at $x_2 = h$. The local polar coordinates used in Eqs.22 and 23 are then unchanged.

In a moiré experiment, the fringe order, N, is measured at a point in the material. The fringe order is then related to the displacement at that point by

$$u_j = N_j p,$$

where $j = 1$ or $j = 2$ depending on which displacement component is measured, and p is the pitch of the moiré grating. Over the field of interest in the bimaterial, we then have from the moiré experiment data of the form $(x_1^i, x_2^i, u_1^i, u_2^i)$, $i = 1, 2, \ldots, 2\mathcal{M}$ where we assume that we have $\mathcal{M}$ data points in each of material A and material B.

If the moiré data is obtained in material B, $x_2^i < h$, and we obtain both displacements u_1 and u_2 at each point (x_1^i, x_2^i), then we use Eqs. 22 and 23 and write

$$Eu_1^B(r_i, \theta_i) = \sum_{j=0}^{J} r_i^{j+1/2} \left[A_j\ f_j(\theta_i) + C_j\ p_j(\theta_i)\right] + \sum_{m=0}^{M} r_i^{m+1} \left[B_m\ g_m(\theta_i) + D_m\ q_m(\theta_i)\right], \tag{32}$$

$$Eu_2^B(r_i, \theta_i) = \sum_{j=0}^{J} r_i^{j+1/2} \left[A_j\ h_j(\theta_i) + C_j\ s_j(\theta_i)\right] + \sum_{m=0}^{M} r_i^{m+1} \left[B_m\ k_m(\theta_i) + D_m\ t_m(\theta_i)\right], \tag{33}$$

where (r_i, θ_i) is obtained from the Cartesian coordinates (x_1^i, x_2^i). For the $\mathcal{M}$ data points in the cracked portion of the bimaterial we then have the $2\mathcal{M} \times 2(J + M + 2)$ linear system,

$$\begin{bmatrix} \mathbf{u}_1^B \\ \mathbf{u}_2^B \end{bmatrix} = \begin{bmatrix} \mathcal{W}_{11} & \mathcal{W}_{12} & \mathcal{W}_{13} & \mathcal{W}_{14} \\ \mathcal{W}_{21} & \mathcal{W}_{22} & \mathcal{W}_{23} & \mathcal{W}_{24} \end{bmatrix} \begin{bmatrix} \mathbf{A} \\ \mathbf{B} \\ \mathbf{C} \\ \mathbf{D} \end{bmatrix}, \tag{34}$$

where the submatrices $\mathcal{W}_{\mathrm{IJ}}$ have elements given through Eqs. 22 and 23 as

$$\begin{aligned} \mathcal{W}_{11_{mn}} &= r_m^{n-1/2}\ f_{n-1}(\theta_m) & \mathcal{W}_{21_{mn}} &= r_m^{n-1/2}\ h_{n-1}(\theta_m) \\ \mathcal{W}_{12_{mn}} &= r_m^{n}\ g_{n-1}(\theta_m) & \mathcal{W}_{22_{mn}} &= r_m^{n}\ k_{n-1}(\theta_m) \\ \mathcal{W}_{13_{mn}} &= r_m^{n-1/2}\ p_{n-1}(\theta_m) & \mathcal{W}_{23_{mn}} &= r_m^{n-1/2}\ s_{n-1}(\theta_m) \\ \mathcal{W}_{14_{mn}} &= r_m^{n}\ q_{n-1}(\theta_m) & \mathcal{W}_{24_{mn}} &= r_m^{n}\ t_{n-1}(\theta_m). \end{aligned}$$

Finally, we note that the linear system of Eq. 34 is overdetermined, with $2\mathcal{M} > 2(J + M + 2)$.

Now consider the moiré data obtained in material A, $x_2^i > h$, and again we obtain both displacements u_1 and u_2 at each point (x_1^i, x_2^i). For the MFS calculation, we consider the point sources to be applied on a line located outside of material A a distance d below the interface at $x_2 = h - d$. The point sources then have coordinates $Q_n = (x_1^n, h - d)$ and the calculation points have coordinates $P_i = (x_1^i, x_2^i)$. We then use Eqs. 7 and 8 and write

$$u_1^A(P_i) = \sum_{n=1}^{N} a_n G_{11}(P_i, Q_n) + \sum_{n=1}^{N} b_n G_{12}(P_i, Q_n), \tag{35}$$

$$u_2^A(P_i) = \sum_{n=1}^{N} a_n G_{21}(P_i, Q_n) + \sum_{n=1}^{N} b_n G_{22}(P_i, Q_n). \tag{36}$$

For the $\mathcal{M}$ data points in the uncracked portion of the bimaterial we then have the $2\mathcal{M} \times 2N$ linear system,

$$\begin{bmatrix} \mathbf{u}_1^A \\ \mathbf{u}_2^A \end{bmatrix} = \begin{bmatrix} \mathcal{G}_{11} & \mathcal{G}_{12} \\ \mathcal{G}_{21} & \mathcal{G}_{22} \end{bmatrix} \begin{bmatrix} \mathbf{a} \\ \mathbf{b} \end{bmatrix}, \tag{37}$$

where the submatrices $\mathcal{G}_{\mathrm{IJ}}$ have elements given through Eqs. 7 and 8 as

$$\begin{aligned} \mathcal{G}_{11_{mn}} &= G_{11}(P_m, Q_n) & \mathcal{G}_{12_{mn}} &= G_{12}(P_m, Q_n), \\ \mathcal{G}_{21_{mn}} &= G_{21}(P_m, Q_n) & \mathcal{G}_{22_{mn}} &= G_{22}(P_m, Q_n). \end{aligned}$$

At the interface, $x_2 = h$, the traction and displacement are continuous,

$$\begin{aligned} t_1(x_1, h^+) - t_1(x_1, h^-) &= 0 \\ t_2(x_1, h^+) - t_2(x_1, h^-) &= 0, \end{aligned} \tag{38}$$

$$\begin{aligned} u_1(x_1, h^+) - u_1(x_1, h^-) &= 0 \\ u_2(x_1, h^+) - u_2(x_1, h^-) &= 0, \end{aligned} \tag{39}$$

where the terms evaluated at $x_2 = h^+$ are formed from the MFS expansions and the terms evaluated at $x_2 = h^-$ are formed using the generalized Westergaard expansions. In order to form these expressions, we first need the traction components, $t_i = \sigma_{ij} n_j$, where σ_{ij} is the stress tensor and n_j is the local normal vector. From the MFS expansions of Eqs. 7 and 8, we then obtain for the tractions in material A,

$$t_1^A(P) = \sum_{n=1}^{N} \left[a_n\, \delta_n(P, Q_n) + b_n\, \zeta_n(P, Q_n)\right], \quad (40)$$

$$t_2^A(P) = \sum_{n=1}^{N} \left[a_n\, \xi_n(P, Q_n) + b_n\, \rho_n(P, Q_n)\right], \quad (41)$$

where

$$\begin{aligned}
\delta_n(P, Q_n) = &\left\{\frac{2\mu(1-\nu)}{1-2\nu}\frac{\partial G_{11}}{\partial x_1} + \frac{2\mu\nu}{1-2\nu}\frac{\partial G_{12}}{\partial x_2}\right\} n_1 \\
&+ \left\{\mu\frac{\partial G_{11}}{\partial x_2} + \mu\frac{\partial G_{12}}{\partial x_1}\right\} n_2, \\
\zeta_n(P, Q_n) = &\left\{\frac{2\mu(1-\nu)}{1-2\nu}\frac{\partial G_{21}}{\partial x_1} + \frac{2\mu\nu}{1-2\nu}\frac{\partial G_{22}}{\partial x_2}\right\} n_1 \\
&+ \left\{\mu\frac{\partial G_{21}}{\partial x_2} + \mu\frac{\partial G_{22}}{\partial x_1}\right\} n_2, \\
\xi_n(P, Q_n) = &\left\{\mu\frac{\partial G_{11}}{\partial x_2} + \mu\frac{\partial G_{12}}{\partial x_1}\right\} n_1 \\
&+ \left\{\frac{2\mu\nu}{1-2\nu}\frac{\partial G_{11}}{\partial x_1} + \frac{2\mu(1-\nu)}{1-2\nu}\frac{\partial G_{12}}{\partial x_2}\right\} n_2, \\
\rho_n(P, Q_n) = &\left\{\mu\frac{\partial G_{21}}{\partial x_2} + \mu\frac{\partial G_{22}}{\partial x_1}\right\} n_1 \\
&+ \left\{\frac{2\mu\nu}{1-2\nu}\frac{\partial G_{21}}{\partial x_1} + \frac{2\mu(1-\nu)}{1-2\nu}\frac{\partial G_{22}}{\partial x_2}\right\} n_2,
\end{aligned}$$

where the derivatives of G_{ij} are evaluated at (P, Q_n) and, for the case of a planar interface along the x_1 axis, $n = (0,\ 1)^T$. Similarly, from the definition of the generalized Westergaard stresses given by Eqs. 10–12 and Eqs. 15–17, and the expansions Eqs. 20–21, we obtain the tractions in material B

$$\begin{aligned}
t_1^B(r, \theta) = &\sum_{j=0}^{J} r^{j-1/2} \left[A_j\, \beta_j(\theta) + C_j\, \eta_j(\theta)\right] \\
&+ \sum_{m=0}^{M} r^m \left[B_m\, \gamma_m(\theta) + D_m\, \kappa_m(\theta)\right], \quad (42)
\end{aligned}$$

$$\begin{aligned}
t_2^B(r, \theta) = &\sum_{j=0}^{J} r^{j-1/2} \left[A_j\, \phi_j(\theta) + C_j\, \psi_j(\theta)\right] \\
&+ \sum_{m=0}^{M} r^m \left[B_m\, \chi_m(\theta) + D_m\, \omega_m(\theta)\right], \quad (43)
\end{aligned}$$

where

$$\begin{aligned}
\beta_j(\theta) = n_1 &\left[\cos\left(j-\frac{1}{2}\right)\theta \right.\\
&\left. -\left(j-\frac{1}{2}\right)\sin\theta\,\sin\left(j-\frac{3}{2}\right)\theta\right] \\
&-n_2\left(j-\frac{1}{2}\right)\sin\theta\,\cos\left(j-\frac{3}{2}\right)\theta \\
\gamma_m(\theta) = &-n_1\left[m\ \sin\theta\,\sin(m-1)\theta - 2\cos m\theta\right] \\
&+n_2\left[\sin m\theta + m\sin\theta\,\cos(m-1)\theta\right] \\
\eta_j(\theta) = n_1 &\left[\left(j-\frac{1}{2}\right)\sin\theta\,\cos\left(j-\frac{3}{2}\right)\theta\right. \\
&\left. +2\sin\left(j-\frac{1}{2}\right)\theta\right] \\
&-n_2\left[\left(j-\frac{1}{2}\right)\sin\theta\,\sin\left(j-\frac{3}{2}\right)\theta\right. \\
&\left. +\cos\left(j-\frac{1}{2}\right)\theta\right] \\
\kappa_m(\theta) = &\ n_1\left[\sin m\theta + m\sin\theta\,\cos(m-1)\theta\right] \\
&-n_2\, m\ \sin\theta\,\sin(m-1)\theta \\
\phi_j(\theta) = &-n_1\left(j-\frac{1}{2}\right)\sin\theta\,\cos\left(j-\frac{1}{2}\right)\theta \\
&+n_2\left[\cos\left(j-\frac{1}{2}\right)\theta\right. \\
&\left. +\left(j-\frac{1}{2}\right)\sin\theta\,\sin\left(j-\frac{3}{2}\right)\theta\right] \\
\chi_m(\theta) = &-n_1\left[\sin m\theta + m\sin\theta\,\cos(m-1)\theta\right] \\
&+n_2\, m\sin\theta\,\sin(m-1)\theta \\
\psi_j(\theta) = n_1 &\left[-\left(j-\frac{1}{2}\right)\sin\theta\,\sin\left(j-\frac{3}{2}\right)\theta\right. \\
&\left. +\cos\left(j-\frac{1}{2}\right)\theta\right] \\
&-n_2\left(j-\frac{1}{2}\right)\sin\theta\,\cos\left(j-\frac{3}{2}\right)\theta \\
\omega_m(\theta) = &-n_1\, m\sin m\theta\,\sin(m-1)\theta \\
&+n_2\left[\sin(m-1)\theta\right. \\
&\left. -m\sin\theta\,\cos(m-1)\theta\right].
\end{aligned}$$

Selecting $\mathcal{N}$ collocation points along the interface, $\left[(x_1^i, h)\right]_{i=1}^{\mathcal{N}}$, we then write for the traction continuity of

Eq. 38, using Eqs. 40–43, and the displacement continuity of Eq. 39, using Eqs. 7–8 and Eqs. 22–23,

$$\begin{bmatrix} \mathbf{0} \\ \mathbf{0} \\ \mathbf{0} \\ \mathbf{0} \end{bmatrix} = \begin{bmatrix} \mathcal{A}_{11} & \mathcal{A}_{12} & \mathcal{A}_{13} & \mathcal{A}_{14} & \mathcal{A}_{15} & \mathcal{A}_{16} \\ \mathcal{A}_{21} & \mathcal{A}_{22} & \mathcal{A}_{23} & \mathcal{A}_{24} & \mathcal{A}_{25} & \mathcal{A}_{26} \\ \mathcal{A}_{31} & \mathcal{A}_{32} & \mathcal{A}_{33} & \mathcal{A}_{34} & \mathcal{A}_{35} & \mathcal{A}_{36} \\ \mathcal{A}_{41} & \mathcal{A}_{42} & \mathcal{A}_{43} & \mathcal{A}_{44} & \mathcal{A}_{45} & \mathcal{A}_{46} \end{bmatrix} \begin{bmatrix} \mathbf{a} \\ \mathbf{b} \\ \mathbf{A} \\ \mathbf{B} \\ \mathbf{C} \\ \mathbf{D} \end{bmatrix} \tag{44}$$

which is a $4\mathcal{N} \times 2(N + J + M + 2)$ linear system. The submatrices $\mathcal{A}_{\mathrm{IJ}}$ are

$$\begin{aligned}
\mathcal{A}_{11_{mn}} &= \delta_n(P_m, Q_n) & \mathcal{A}_{12_{mn}} &= \zeta_n(P_m, Q_n) \\
\mathcal{A}_{13_{mn}} &= -r_m^{n-3/2}\ \beta_{n-1}(\theta_m) & \mathcal{A}_{14_{mn}} &= -r_m^{n-2}\gamma_{n-1}(\theta_m) \\
\mathcal{A}_{15_{mn}} &= -r_m^{n-3/2}\ \eta_{n-1}(\theta_m) & \mathcal{A}_{16_{mn}} &= -r_m^{n-2}\ \kappa_{n-1}(\theta_m) \\
\mathcal{A}_{21_{mn}} &= \xi_n(P_m, Q_n) & \mathcal{A}_{22_{mn}} &= \rho_n(P_m, Q_n) \\
\mathcal{A}_{23_{mn}} &= -r_m^{n-3/2}\ \phi_{n-1}(\theta_m) & \mathcal{A}_{24_{mn}} &= -r_m^{n-2}\chi_{n-1}(\theta_m) \\
\mathcal{A}_{25_{mn}} &= -r_m^{n-3/2}\ \psi_{n-1}(\theta_m) & \mathcal{A}_{26_{mn}} &= -r_m^{n-2}\ \omega_{n-1}(\theta_m) \\
\mathcal{A}_{31_{mn}} &= \mathcal{G}_{11_{mn}} & \mathcal{A}_{32_{mn}} &= \mathcal{G}_{12_{mn}} \\
\mathcal{A}_{33_{mn}} &= -\mathcal{W}_{11_{mn}} & \mathcal{A}_{34_{mn}} &= -\mathcal{W}_{12_{mn}} \\
\mathcal{A}_{35_{mn}} &= -\mathcal{W}_{13_{mn}} & \mathcal{A}_{36_{mn}} &= -\mathcal{W}_{14_{mn}} \\
\mathcal{A}_{41_{mn}} &= \mathcal{G}_{21_{mn}} & \mathcal{A}_{42_{mn}} &= \mathcal{G}_{22_{mn}} \\
\mathcal{A}_{43_{mn}} &= -\mathcal{W}_{21_{mn}} & \mathcal{A}_{44_{mn}} &= -\mathcal{W}_{22_{mn}} \\
\mathcal{A}_{45_{mn}} &= -\mathcal{W}_{23_{mn}} & \mathcal{A}_{46_{mn}} &= -\mathcal{W}_{24_{mn}}
\end{aligned}$$

where $P_m = (x_1^m, h^+)$, $Q_n = (x_1^n, h - d)$ and (r_m, θ_m) is computed from (x_1^m, h^-).

Combining the linear systems of Eqs. 34, 37, and 44 yields the $4(\mathcal{M} + \mathcal{N}) \times 4(N + J + M + 2)$ overdetermined linear system

$$\begin{bmatrix} \mathbf{u}_1^A \\ \mathbf{u}_2^A \\ \mathbf{u}_1^B \\ \mathbf{u}_2^B \\ \mathbf{0} \\ \mathbf{0} \\ \mathbf{0} \\ \mathbf{0} \end{bmatrix} = \begin{bmatrix} \mathcal{G}_{11} & \mathcal{G}_{12} & 0 & 0 & 0 & 0 \\ \mathcal{G}_{21} & \mathcal{G}_{22} & 0 & 0 & 0 & 0 \\ 0 & 0 & \mathcal{W}_{11} & \mathcal{W}_{12} & \mathcal{W}_{13} & \mathcal{W}_{14} \\ 0 & 0 & \mathcal{W}_{21} & \mathcal{W}_{22} & \mathcal{W}_{23} & \mathcal{W}_{24} \\ \mathcal{A}_{11} & \mathcal{A}_{12} & \mathcal{A}_{13} & \mathcal{A}_{14} & \mathcal{A}_{15} & \mathcal{A}_{16} \\ \mathcal{A}_{21} & \mathcal{A}_{22} & \mathcal{A}_{23} & \mathcal{A}_{24} & \mathcal{A}_{25} & \mathcal{A}_{26} \\ \mathcal{A}_{31} & \mathcal{A}_{32} & \mathcal{A}_{33} & \mathcal{A}_{34} & \mathcal{A}_{35} & \mathcal{A}_{36} \\ \mathcal{A}_{41} & \mathcal{A}_{42} & \mathcal{A}_{43} & \mathcal{A}_{44} & \mathcal{A}_{45} & \mathcal{A}_{46} \end{bmatrix} \begin{bmatrix} \mathbf{a} \\ \mathbf{b} \\ \mathbf{A} \\ \mathbf{B} \\ \mathbf{C} \\ \mathbf{D} \end{bmatrix}. \tag{45}$$

The system of Eq. 45 can be solved with standard linear least-squares procedures to obtain estimates for the parameters $(\mathbf{a}, \mathbf{b}, \mathbf{A}, \mathbf{B}, \mathbf{C}, \mathbf{D})^T$. Here, we use the QR decomposition as discussed in Longley (1984).

5 Proof-of-principle numerical experiments

To investigate the proposed analysis procedure, synthetic moiré data was generated for the symmetric (mode I) crack problem shown in Fig. 2. To generate the synthetic displacement data, a boundary element analysis based on a bimaterial Green's function (Berger 1994) was used. The use of a bimaterial Green's function in the boundary element analysis allows only the remote boundaries of the specimen to be discretized. The continuity conditions for displacement and traction across the interface are enforced analytically by the Green's function so no discretization of the interface is required.

The computational domain shown in Fig. 2 was used for the analysis. Since the problem is symmetric, the crack was modelled using symmetry boundary conditions. Additionally, the crack-tip was fixed so that $u_1 = u_2 = 0$. The problem is mode I only, so $\mathbf{C} = \mathbf{D} = 0$ in Eq. 45. The elastic constants of the bimaterial were taken to be equivalent to those of the copper–tungsten (Cu–W) composite used in the experiments discussed in the next section. Specifically, material A is 80% Cu, 20% W, which has a modulus E_A=160 GPa and a Poisson's ratio $\nu_A = 0.330$ and material B is 40% Cu, 60% W which has E_B=190 GPa and ν_B=0.286 (Chapa-Cabrera 2002). Displacements were obtained in the region indicated in Fig. 2. Both u_1 and u_2 were calculated at each point in the region shown.

The displacement data was collocated using the formulation outlined in the previous section. The same number of unknown coefficients were used in the Westergaard and MFS expansions, so $N = J + M + 2$. As we assumed in the formulation, the same number of displacement data points were taken in material A as in material B yielding a total of $4\mathcal{M}$ displacement data points. To emphasize the abundance of moiré data, we select fewer than $\mathcal{M}$ data points along the interface to evaluate Eq. 44; namely, we take $\mathcal{N} = 0.25\mathcal{M}$. The numerical experiments reported on in Barker et al. (1985) suggest using roughly 10 times as many data points as unknown coefficients for good convergence, so we choose $10(\mathcal{M} + \mathcal{N}) = N + J + M + 2$.

The results of the combined Westergaard-MFS collocation are shown in Figs. 3 and 4. In Fig. 3, we have plotted the opening mode stress intensity factor, K_{I}, as a function of the total number of coefficients $N + J + M + 2$. We see from the figure that good convergence is obtained for K_{I} at approximately eight

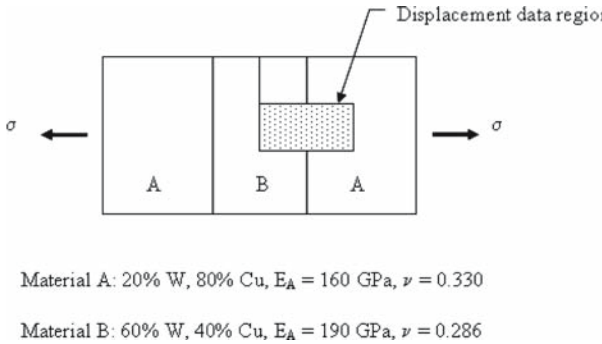

Fig. 2 Copper–tungsten model specimen showing the region of u_1, u_2 calculation

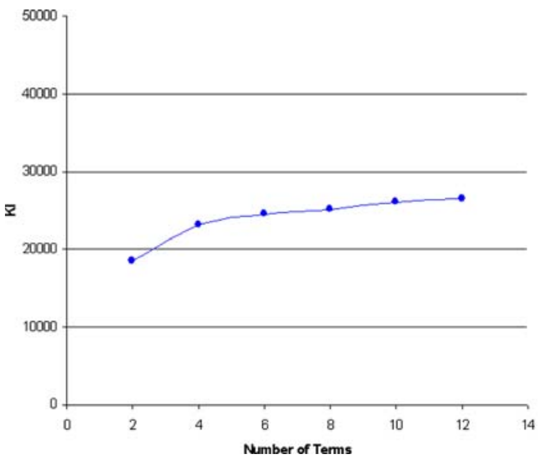

Fig. 3 Convergence of K_{I} from the collocation of the boundary element data

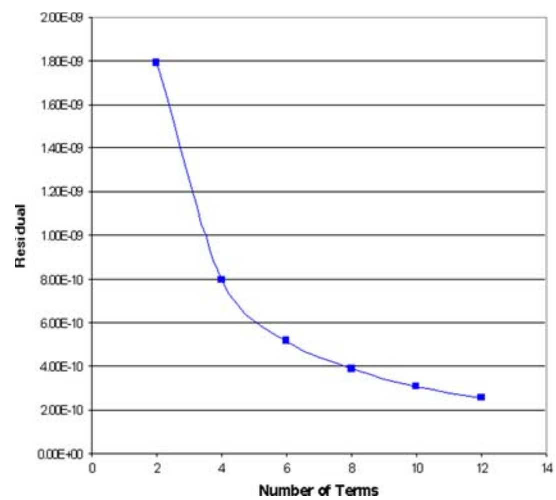

Fig. 4 Residual from the collocation of the boundary element data

coefficients. In Fig. 4 the least squares residual is plotted again as a function of the total number of unknown coefficients. Using 8 coefficients we see the residual is approximately 4.0×10^{-10}. Of course these numerical experiments used perfect displacement data and good results can be expected. The success of the numerical investigation provided confidence to apply the analysis method to actual experimental data. This analysis is discussed in the next section.

6 Application to a Cu–W specimen

Based on the successful application of the analysis method to the synthetic boundary element data, the data analysis methodology presented in this paper was used to extract stress intensity information from experiments performed on copper–tungsten composite specimens. The geometry of the Cu–W composite specimen is shown in Fig. 5. The specimens were fabricated by sintering through hot pressing, described in detail elsewhere (Chapa-Cabrera and Reimanis 2002). Four-point bend bars (3 mm × 8 mm × 30 mm) were machined from the hot-pressed specimens with electro-discharge machining. A notch of length 3 mm was then machined into the specimen. A 1200 line/mm aluminized grating was fixed to the surface of the four-point bend bar with epoxy. Sharp precracks were grown at the base of the notch in each specimen by fatigue, parallel to the 8 mm dimension. Each specimen was then loaded in four-point bending until the crack extended.

Phase-shifted moiré intereferometry (PSMI) was used to collect the crack-tip displacement field, similar to experiments described in Steffler 2001. A typical fringe pattern obtained for the u_1-field is shown in Fig. 6. The displacement data generated with PSMI were analyzed using the Westergaard-MFS algorithm to extract the stress field parameters. Figures 7 and 8

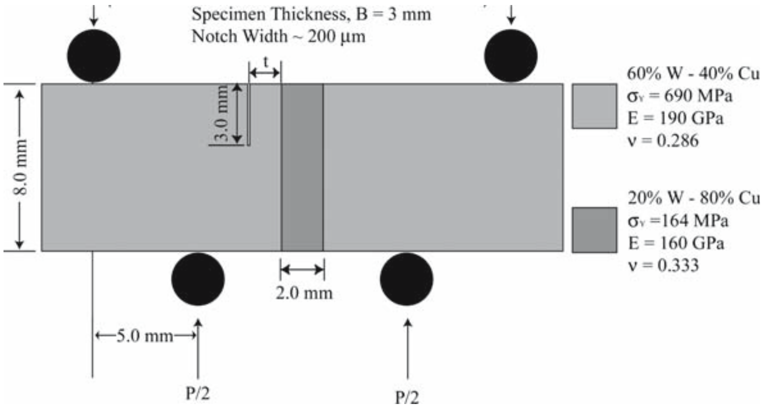

Fig. 5 Copper–tungsten specimen

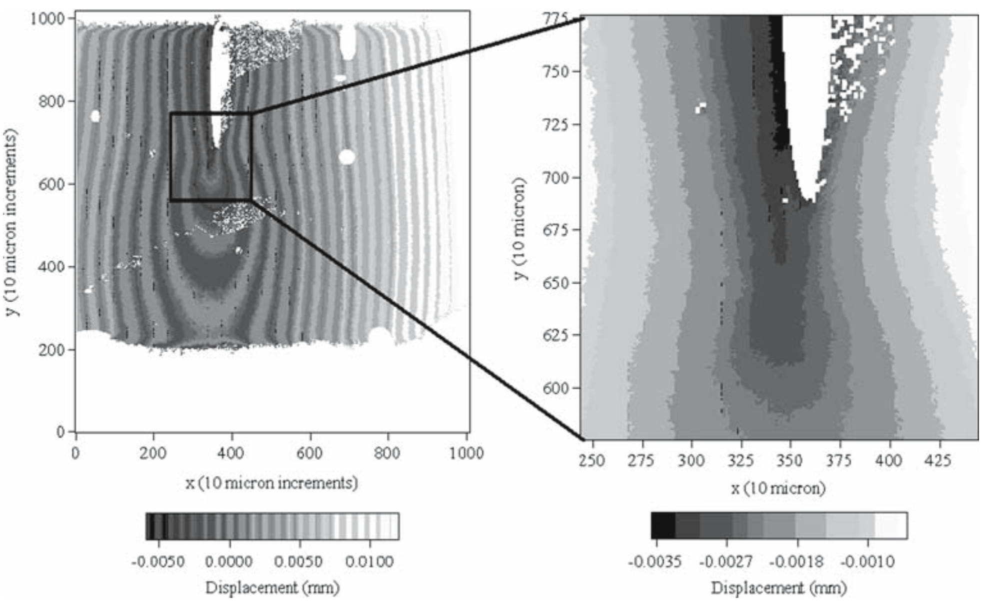

Fig. 6 Phase-shifted moiré fields for the u_1-displacement obtained in the copper–tungsten specimen

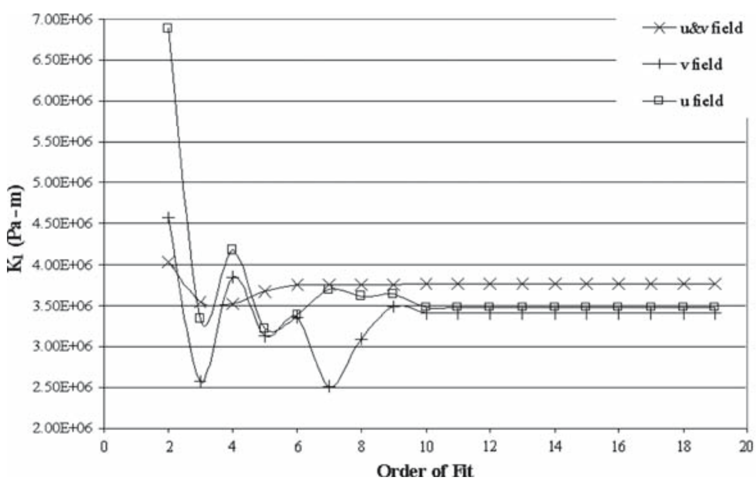

Fig. 7 Convergence of K_I from collocation of the experimental moiré data

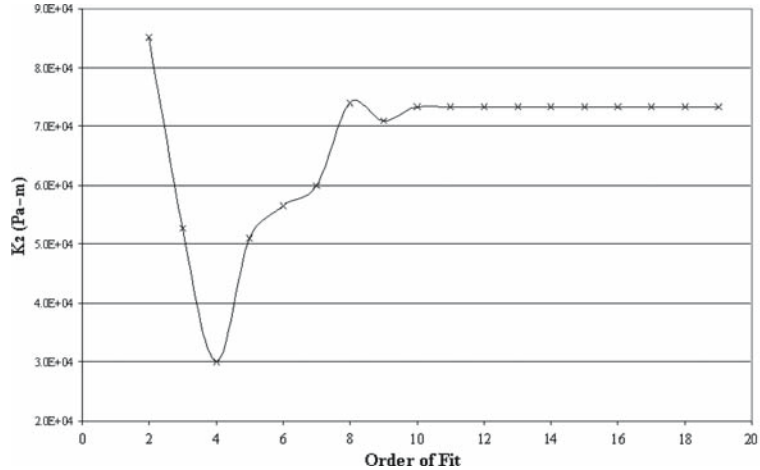

Fig. 8 Convergence of K_{II} from collocation of the experimental moiré data

illustrate the convergence of K_{I} and K_{II} as a function of the number of unknowns in the series expansions. Each figure shows the results of the collocation using data from the u_1 and u_2 fields individually as well as the combined u_1 and u_2 fields. The results from the combined fields shows convergence to a slightly higher value of K_{I} than the results using the individual fields, consistent with results in Sanford (2003); it is likely that the increased redundancy in the combined data from both u_1 and u_2 fields leads to higher accuracy. The plot for K_{II} shows only the combined u_1 and u_2 fields.

K_{IC} measured for the 60%W–40%Cu composition is $4.5\,\mathrm{MPa}\cdot\sqrt{\mathrm{m}}$. The K_{I} value measured in the same composition here is approximately $4\ \mathrm{MPa}\cdot\sqrt{\mathrm{m}}$. This value is lower because the displacement field is taken after the crack has arrested and thus, K_{I} should be lower than K_{IC}. K_{II} is expected to be orders of magnitude lower than K_{I} because the crack is extending under mode I conditions and a $K_{\mathrm{II}} = 0$ fracture criterion should apply.

7 Summary

In this paper we have developed a method applicable to the analysis of moiré data obtained in cracked bimaterial specimens. The analysis technique allows the use of displacement data obtained in the uncracked portion of the bimaterial by using expansions from the MES Coupling these expansions with the usual Westergaard crack-tip expansions allows one to take full advantage of the data available from a moiré experiment. Our numerical results indicated the methodology worked well on synthetic data generated from a boundary element analysis, and the application of the methodology to actual experimental data was successful. Although both example problems investigated here contained a planar interface, the method can easily be used on problems with curved interfaces.

Acknowledgements The authors acknowledge the support of the Army Research Office, grant number DAAD19-01-1-0590, to the Colorado School of Mines. The use of the moiré facilities at the Idaho National Laboratories and the assistance of Dr. Eric Steffler of INL are gratefully acknowledged.

References

Barker DB, Sanford RJ, Chona R (1985) Determining K and related stress-field parameters from displacement fields. Exp Mech 25:399–407

Berger JR (1994) Boundary element analysis of anisotropic bimaterials with special Green's functions. Eng Anal Boundary Elements 14:123–131

Berger JR, Karageorghis A (2001) The method of fundamental solutions for elastic layered materials. Eng Anal Boundary Elements 25:877–886

Chapa-Cabrera J (2002) Fracture and deformation in Cu/W graded joints. Ph.D. dissertation, Colorado School of Mines

Chapa-Cabrera J, Reimanis I (2002) Crack deflection in compositionally graded Cu–W composites. Phil Mag A 82:3393–3403

Dally JW (1979) Dynamic photoelastic studies of fracture. Exp Mech 19:349–361

Dally JW, Read DT (1993) Electron beam moiré . Exp Mech 33:270–277

Drexler ES, Berger JR (1999) Mechanical deformation in conductive adhesives measured with electron-beam moiré . J Electron Packaging 121:69–74

Epstein JS, Dadkhah MS (1993) Moiré interferometry in fracture research. Chapter 11. In: Epstein JS (ed) Experimental techniques in fracture. VCH Publishers, New York, pp 427–508

Etheridge JM, Dally JW (1977) A critical review of methods for determining the stress intensity factor from isochromatic fringes. Exp Mech 17:248–254

Fairweather G, Karageorghis A (1998) The method of fundamental solutions for elliptic boundary value problems. Adv Comput Math 9:69–95

Golberg MA, Chen CS (1999) The method of fundamental solutions for potential, Helmholtz and diffusion problems. Chapter 4. In: Golberg MA (ed) Boundary integral methods: numerical and mathematical aspects. WIT Press and Computational Mechanics Publications, Boston, pp 105–176

Kalthoff JF (1987) Shadow optical method of caustics. In: Kobayashi AS (ed) Handbook on experimental mechanics. McGraw-Hill Publishers, New York, NY, pp 430–498

Longley JW (1984) Least squares computations using orthogonalization methods. Marcel Dekker, Inc., New York, NY

Poullikkas A, Karageorghis A, Georgiou G (1998) Methods of fundamental solutions for harmonic and biharmonic boundary value problems. Comput Mech 21:416–423

Read DT, Dally JW (1994) Electron-beam moiré study of fracture of a glass fiber reinforced plastic composite. J Appl Mech 61:402–409

Rosakis AJ, Zehnder AT (1985) On the method of caustics: an exact analysis based on geometrical optics. J Elasticity 4:347–367

Sanford RJ, Dally JW (1979) A general method for determining mixed-mode stress intensity factors from isochromatic fringe patterns. Eng Fract Mech 11:621–633

Sanford RJ (1979) A critical re-examination of the Westergaard method for solving opening mode crack problems. Mech Res Commun 6:289–294

Sanford RJ (2003) Principles of fracture mechanics. Prentice Hall/Pearson Education, Upper Saddle River, New Jersey

Schroedl MA, Smith CW (1975) A study of near and far field effects in photoelastic stress intensity determination. Eng Frac Mech 7:341–355

Steffler ED (2001) Applications of phase shifted moiré interferometry. In: Trumble K, Bowman K, Reimanis I, Sampath S (eds) Ceramic transactions, vol 114: Functionally grade materials 2000. Published by the American Ceramic Society, Westerville, OH pp 595–602

Theocaris PS, Gdoutos E (1972) An optical method for determining opening-mode and edge-sliding-mode stress-intensity factors. J Appl Mech 39:91–97

Westergaard HM (1939) Bearing pressures and cracks. J Appl Mech 6:A49–A53

Williams ML (1957) On the stress distribution at the base of a stationary crack. J Appl Mech 24:109–114